Available online at www.sciencedirect.com
SCIENCE DIRECT
International Journal of Thermal Sciences 45 (2006) 848–859
International Journal of Thermal Sciences
www.elsevier.com/locate/ijts

Evaluation of smoke dispersion from forest fire plumes using lidar experiments and modelling

Alexander Lavrov [a], Andrei B. Utkin [a], Rui Vilar [b,*], Armando Fernandes [b]

[a] *INOV-INESC-Inovação, Rua Alves Redol, 9, 1000-029, Lisbon, Portugal*
[b] *Departamento de Engenharia de Materiais, Instituto Superior Técnico, Av. Rovisco Pais, 1, 1049-001, Lisbon, Portugal*

Received 22 March 2005; received in revised form 16 December 2005; accepted 3 January 2006

Available online 24 February 2006

Abstract

The dispersion of forest fire smoke was studied using direct-detection lidar measurements and a Reynolds-averaged Navier–Stokes fluid dynamics model. Comparison between experimental and theoretical results showed that the model adequately describes the influence of the main factors affecting the dispersion of a hot smoke plume in the presence of wind, taking into consideration turbulent mixing, the influence of wind, and the action of buoyancy, and proved that lidar measurements are an appropriate tool for the semiqualitative analysis of forest fire smoke plume evolution and prediction of lidar sensitivity and range for reliable smoke detection. It was also demonstrated that analysis of lidar signals using Klett's inversion method allows the internal three-dimensional structure of the smoke plumes to be semiquantitatively determined and the absolute value of smoke-particle concentration to be estimated.

Keywords: Forest fire detection; Smoke; Plume; Computational fluid dynamics; Lidar

1. Introduction

Coherent laser radiation has been used effectively for many decades to investigate momentum, heat, and mass transfer in fluid dynamics [1]. In particular, lidar (laser radar, LIght Detection And Ranging) has been applied for analysing contrails (the condensation trail of an aircraft engine) [2], for studying plume rise and dispersion, and for estimating particle concentrations in smoke plumes [3–8].

The principles of lidar operation are analogous to radar; it uses measurements of backscattered radiation intensity for environmental remote sensing to detect and track objects in the atmosphere [9]. The lidar emitter is a pulsed laser providing short pulses of intense monochromatic radiation in the spectral range between ∼200 and 11 000 nm. The receiver consists of a light-gathering optical device (usually a telescope) that directs radiation to a photodetector (photomultiplier or photodiode) connected to a computer-controlled data acquisition system. When the laser emits pulses of the radiation in the target's direction, part of this radiation is backscattered by the target and collected by the receiver. In the simplest case of a single-wavelength direct-detection lidar, the temporal dependence of the backscattered radiation power (converted into an electrical signal by the photodetector and then into a digital array by the data acquisition system)—the raw lidar signal—is used to retrieve the target position and other parameters. As a rule, the simplest lidar methods are not sufficiently sensitive to characterise molecular interaction, and it is solid and/or particulate-matter targets that can be successfully investigated using this technique. Specifically, direct-detection lidar provides information on particle distribution in aerosols and smoke plumes, and early fire detection and automatic forest-fire surveillance are among its prospective applications [6–10], competing with passive methods based on IR and video imaging [11].

Although other techniques such as laser-Doppler velocimetry (LDV) and laser-induced fluorescence (LIF) can measure flow fields [12,13] and restore particle concentration profiles near phase boundaries [14], the direct-detection lidar method was preferred because of its simplicity, low cost, equipment mobility, robustness, and low energy consumption. Following

* Corresponding author.
E-mail address: rui.vilar@ist.utl.pt (R. Vilar).

1290-0729/$ – see front matter
doi:10.1016/j.ijthermalsci.2006.01.003

Nomenclature

B	effective photodetection bandwidth	s^{-1}
c	velocity of light	$m\,s^{-1}$
D	diameter of tower in the experiments of Bornoff and Mokhtarzadeh–Dehghan	mm
D_{rec}	receiver optics diameter	m
e	electron charge	C
E_l	laser pulse energy	J
F	noise factor associated with photomultiplier gain	
Fr	Froude number	
$\vec{g}$	gravity acceleration vector	$m\,s^{-2}$
G	photomultiplier gain	
h	enthalpy	$J\,kg^{-1}$
I_{dark}	photomultiplier dark current	A
k	turbulent kinetic energy	$m^2\,s^{-2}$
L_{per}	perimeter of rectangular burning area	m
n	smoke particle concentration	m^{-3}
n^*	complex refraction index of smoke particle	
n_s	number of accumulated lidar signals	
N	smoke particle size distribution	m^{-4}
p	pressure	Pa
P_{rec}	power collected by lidar receiver	W
P_{bgnd}	power of received background solar radiation	W
Pr	turbulent Prandtl number	
r	smoke particle radius	m
R	distance from radiation source to target	m
R_{ph}	photomultiplier photocathode responsivity	$A\,W^{-1}$
S_1, S_2, S_3	square of burning area	m^2
SNR	lidar signal-to-noise ratio	
t_p	laser pulse duration	s
t_{max}	total fire duration	s
T	temperature	K
u_1, u_2, u_3	velocity components	$m\,s^{-1}$
u_{wind}	wind speed	$m\,s^{-1}$
x_1, x_2, x_3	Cartesian coordinates	m

Greek symbols

α	air extinction coefficient	m^{-1}
β	backscattering coefficient of smoke	$m^{-1}\,sr^{-1}$
ε	rate of dissipation of turbulent energy	$m^2\,s^{-3}$
θ_B	Mie backscattering efficiency	sr^{-1}
λ	laser wavelength	m
μ_{eff}	viscosity	$kg\,m^{-1}\,s^{-1}$
μ_{lam}	laminar viscosity	$kg\,m^{-1}\,s^{-1}$
μ_t	turbulent viscosity	$kg\,m^{-1}\,s^{-1}$
ρ	density	$kg\,m^{-3}$
τ_{rec}	receiver efficiency	
τ_{tr}	transmitter efficiency	

Subscripts

bgnd	background solar radiation
eff	effective
fin	final
l	laser
lam	laminar
p	laser pulse
ph	photomultiplier
per	perimeter of burning area
rec	receiver
s	signal
t	turbulent
tr	transmitter

recent developments in manufacturing industrial and military laser rangefinders (which in fact are direct-detection lidars coupled with thresholding electronics), the instruments using laser detection and ranging are now robust devices capable of long-term standalone operation rather than special laboratory tools that need frequent checking, adjustment, and retuning by high-qualified personnel. For this reason the lidar technique is one of the first candidates for use in future commercial automatic fire-surveillance systems, and investigation of its accuracy and limitations goes far beyond the scope of pure scientific interest.

The present paper is devoted to estimation of the 3D distribution of particle concentrations in forest fire smoke plumes, based on data derived from two sources: lidar measurements of smoke plumes emanating from experimental forest fires and results of numerical calculations based on the 3D Reynolds-averaged Navier–Stokes equations (hereafter referred to as the Navier–Stokes equations). Here the lidar measurements provide information on the particulate-matter distribution while the numerical model deals with all the combustion products: particulate matter (soot), CO_2, H_2O, nitric oxides, hydrocarbons, and other gases. The linkage between these two data sources is made by the assumption that the structure of the particle-concentration field, $n(x_1, x_2, x_3)$, is similar to the temperature field, $T(x_1, x_2, x_3)$.

An example of such an investigation, in which the particle concentration in smoke plumes was evaluated using lidar experimental results and numerical calculations based on a one-dimensional hydrodynamics "top hat" model, was recently presented by Lavrov et al. [6]. However the "top hat" approximation does not allow the variation of plume parameters in the radial direction to be taken into account, hence the influence of wind cannot be taken into consideration. In the present paper, lidar experimental results are compared with the predictions of a three-dimensional numerical hydrodynamics model based on the Navier–Stokes equations. This comparison allows peculiarities of the smoke plume behaviour to be revealed and plume drift and smoke diffusion in the atmosphere to be studied.

Experimental data of Stith et al. [15] show that the percentage of wood transformed into particulate matter at burning (PWT) varies in the range of 0.2 to 2%. In a previous paper [6] we compared experimental signal-to-noise ratio data for the detection of a small campfire with a burning rate of $\approx 0.025\ kg\,s^{-1}$ with calculated results and used PWT as a fitting parameter to achieve the best agreement between experiment and theory. The

value of PWT which leads to the best agreement, was 0.3%, and this value has been used in the present paper.

2. Formulation of the smoke-plume model

The geometry of the hydrodynamics model is presented in Fig. 1. The hot smoke plume is assumed to result from a rectangular burning area of steady state combustion. The plume rises in the atmosphere due to buoyancy forces, being deflected by the wind and mixed with ambient air.

Usually, models of smoke plumes and jets are based on Reynolds-averaged Navier–Stokes equations (RANS) [16–24], large eddy simulation (LES) [18,24–28], and direct numerical simulations [29]. Frequently the LES technique provides a better description of turbulence-related effects, but requires finer grids and longer computation time than RANS-based models. Moreover, the traditional LES approach based on eddy-viscosity subfilter models has fundamental limitations [18,30]. On the other hand RANS-based schemes are readily available in the PHOENICS software and constantly demonstrate good agreement with experiments [31]. For this reason, the RANS method was chosen for the modelling.

The smoke-plume dynamics is described by a three-dimensional system of Navier–Stokes equations [16–24]:

$$\frac{\partial}{\partial x_j}(\rho u_j) = 0 \tag{1}$$

$$\frac{\partial}{\partial x_j}(\rho u_j u_i) = \frac{\partial}{\partial x_j}\left(\mu_{\text{eff}}\frac{\partial u_i}{\partial x_j}\right) - \frac{\partial p}{\partial x_i} + S_i \tag{2}$$

$$\frac{\partial}{\partial x_j}(\rho u_j h) = \frac{\partial}{\partial x_j}\left(\frac{\mu_{\text{eff}}}{Pr}\frac{\partial h}{\partial x_j}\right) \tag{3}$$

$$\frac{\partial}{\partial x_j}(\rho u_j k) = \frac{\partial}{\partial x_j}\left(\frac{\mu_{\text{eff}}}{\sigma_k}\frac{\partial k}{\partial x_j}\right) + P_t + G - \rho\varepsilon \tag{4}$$

$$\frac{\partial}{\partial x_j}(\rho u_j \varepsilon) = \frac{\partial}{\partial x_j}\left(\frac{\mu_{\text{eff}}}{\sigma_\varepsilon}\frac{\partial \varepsilon}{\partial x_j}\right) + c_1\frac{\varepsilon}{k}(P_t + c_3 G) - c_2\rho\frac{\varepsilon^2}{k} \tag{5}$$

$$S_i = \frac{\partial}{\partial x_1}\left(\mu_{\text{eff}}\frac{\partial u_1}{\partial x_i}\right) + \frac{\partial}{\partial x_2}\left(\mu_{\text{eff}}\frac{\partial u_2}{\partial x_i}\right) + \frac{\partial}{\partial x_3}\left(\mu_{\text{eff}}\frac{\partial u_3}{\partial x_i}\right) - g_i(\rho - \rho_{\text{ref}}) \tag{6}$$

where x_1, x_2, x_3 are the Cartesian coordinates, u_1, u_2, u_3 the velocity components in the corresponding directions, $\vec{g} = (0, 0, -9.81)$ the gravity acceleration vector, ρ density, μ_{eff} viscosity, $\mu_{\text{eff}} = \mu_{\text{lam}} + \mu_t$, μ_{lam} laminar viscosity, μ_t turbulent viscosity, p pressure, h enthalpy, Pr the turbulent Prandtl number, k turbulent kinetic energy, and ε the rate of dissipation of the turbulent energy. The term

$$P_t = \mu_t\frac{\partial u_i}{\partial x_j}\left(\frac{\partial u_i}{\partial x_j} + \frac{\partial u_j}{\partial x_i}\right) \tag{7}$$

describes the turbulence kinetic energy generation, while the term

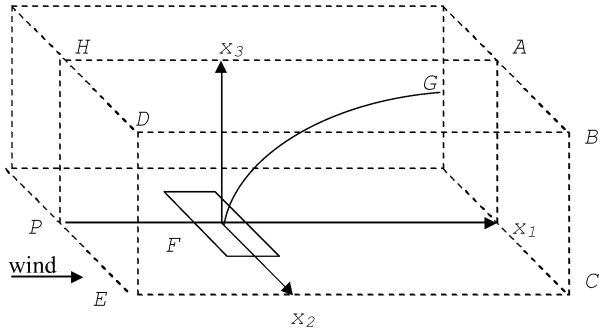

Fig. 1. Computational scheme.

$$G = g_3\frac{\mu_{\text{eff}}}{Pr}\frac{1}{\rho}\frac{\partial \rho}{\partial x_3} \tag{8}$$

takes into account the action of buoyancy forces. The relation between turbulent viscosity and other flow parameters is given by:

$$\mu_t = c_\mu \rho\frac{k^2}{\varepsilon} \tag{9}$$

For the constants appearing in Eqs. (1)–(9) the "classical set" suggested by Launder and Spalding [32] was used: $Pr = 0.7$, $c_1 = 1.44$, $c_2 = 1.92$, $c_3 = 1.00$, $c_\mu = 0.009$, $\sigma_k = 1.0$, and $\sigma_\varepsilon = 1.3$.

The calculation domain is the parallelepiped $PHAx_1EDBC$ (Fig. 1). The centre of the fire plot is F, and the central line of the plume is FG. The flow is symmetrical about the plane $PHAx_1$. The following boundary conditions are imposed:

1. At the left boundary PEDH

Dirichlet conditions:

The horizontal velocity (wind profile) is defined by the equation (see Schlichting [33])

$$u_1(x_3) = u_{\text{wind}}\left(\frac{x_3}{H}\right)^{1/7}$$

where u_{wind} is the wind speed at height H. Following the recommendation of Porterie et al. [34], a height H of 10 m was chosen.

The vertical and transverse velocities are

$$u_2 = u_3 = 0$$

The temperature profile is

$$T_{\text{left}} = T_{\text{air}}$$

Previous calculations by Patankar et al. [19] showed that the final results are insensitive to the value of k_{air} if this value is less than 5% of the kinetic energy of the wind flow and that there is considerable energy associated with the turbulent gas motion near the plume–air boundary. So, it was assumed that

$$k_{\text{left}} \equiv k_{\text{air}} = 0.04\frac{u_1^2}{2}$$

According to Patankar et al. [19] the rate of dissipation of the turbulent energy is

$$\varepsilon_{\text{left}} \equiv \varepsilon_{\text{air}} = 0.001\ \text{m}^2\,\text{s}^{-3}$$

2. At the lower boundary Px_1CE

Outside the plume: adiabatic conditions for T, $\frac{\partial T}{\partial x_3} = 0$, and no-slip conditions for the velocity are specified.

To estimate the turbulent kinetic energy and its rate of dissipation, the wall-function method suggested by Launder and Spalding [32] was used.

Inside the plume:

$$u_3 = u_{\text{jet}}, \qquad u_1 = u_2 = 0, \qquad T = T_{\text{jet}}$$

The turbulent kinetic energy inside the plume is given by:

$$k_{\text{jet}} = 0.01\frac{u_{\text{jet}}^2}{2}$$

and ε is calculated using the equation:

$$\varepsilon_{\text{jet}} = \frac{k_{\text{jet}}^{3/2}}{(L_{\text{per}}/4)}$$

where L_{per} is the perimeter of the rectangular burning area.

3. The back boundary $PHAx_1$ is the symmetry plane of the flow. Consequently, the boundary conditions are:

$$u_2 = 0$$
$$\frac{\partial u_1}{\partial x_2} = \frac{\partial u_3}{\partial x_2} = \frac{\partial T}{\partial x_2} = \frac{\partial k}{\partial x_2} = \frac{\partial \varepsilon}{\partial x_2} = 0$$

4. The front and top boundaries, EDBC and HABD respectively, are assumed to be sufficiently far from the plume for the boundary conditions to correspond to the symmetry conditions:

$$u_2 = 0$$
$$\frac{\partial u_1}{\partial x_2} = \frac{\partial u_3}{\partial x_2} = \frac{\partial T}{\partial x_2} = \frac{\partial k}{\partial x_2} = \frac{\partial \varepsilon}{\partial x_2} = 0$$
$$u_3 = 0$$
$$\frac{\partial u_1}{\partial x_3} = \frac{\partial u_2}{\partial x_3} = \frac{\partial T}{\partial x_3} = \frac{\partial k}{\partial x_3} = \frac{\partial \varepsilon}{\partial x_3} = 0$$

5. For the right boundary x_1ABC the external pressure is given; in this case, in accordance with the SIMPLE algorithm [16,35], it is not necessary to know the boundary conditions for velocity components, and for h, k and ε the "weak" boundary conditions were specified:

$$\frac{\partial h}{\partial x_1} = \frac{\partial k}{\partial x_1} = \frac{\partial \varepsilon}{\partial x_1} = 0$$

Since chemical reactions are not taken into account and acceleration in the plume is relatively low, the traditional approach to smoke modelling can be followed (see, for example, [24]), assuming that the solid phase (ash particles) is generated and transported in such a manner that its temperature and velocity coincide with those of the gas phase. As a result, the particle concentration field $n(x_1, x_2, x_3)$ is similar to the temperature field:

$$\frac{n - n_{\text{air}}}{n_{\text{jet}} - n_{\text{air}}} = \frac{T - T_{\text{air}}}{T_{\text{jet}} - T_{\text{air}}}$$

To solve Eqs. (1)–(9) the SIMPLE (Semi-Implicit Method for Pressure-Linked Equations) computational method (see [16,35]) and PHOENICS 3.6 computational fluid dynamics code [36] were used.

3. PHOENICS code: modelling of a buoyant plume in a wind-induced crossflow

To the best of our knowledge, previously reported computations carried out using the PHOENICS 3.6 code have never been compared with experimental data for the case of mixing of a buoyant plume with a crossflow. In order to validate the model and to demonstrate the applicability of PHOENICS 3.6 code to the modelling of hot-plume behaviour in the presence of a wind-induced crossflow, the computational results were compared with temperature-distribution measurements made by Bornoff and Mokhtarzadeh-Dehghan [24]. Bornoff's experiments were carried out in a wind tunnel. The main air stream with temperature $T_{\text{air}} = 288\,^{\circ}\text{C}$ had a logarithmic velocity profile. Two towers with diameter $D = 33$ mm and height $H = 66$ mm above the wind tunnel floor delivered hot air (temperature $T_{\text{jet}} = 388\,^{\circ}\text{C}$) in the wind stream. The wind velocity at the tower top was $0.39\ \text{m s}^{-1}$. The towers were situated perpendicularly to the wind direction, the distance between the tower centres being 66 mm. The vertical velocity of hot air at the tower exit was $0.91\ \text{m s}^{-1}$. The value of the Froude number for these parameters is $Fr \equiv \frac{u_{\text{jet}}^2}{gD} = 2.6$.

The computations using PHOENICS 3.6 code were performed in the domain $x_1 = 82D$, $x_2 = 24D$, and $x_3 = 28D$ using four different non-uniform grids—$47 \times 37 \times 40$, $59 \times 47 \times 50$, $74 \times 59 \times 63$ and $93 \times 74 \times 79$. The grid is finer near the source and becomes increasingly coarse as the distance to the source increases. A comparison between experimental measurements and calculated results, made on the basis of the dimensionless temperature $T^* = \frac{T - T_{\text{air}}}{T_{\text{jet}} - T_{\text{air}}}$, is presented in Fig. 2.

Good qualitative agreement between experimental and calculated results was observed. Taking into consideration the complexity of this flow/crossflow case study, we can conclude that the PHOENICS 3.6 code is suitable to describe the similar case of a steady-state buoyant smoke flow developed in the presence of a wind-induced crossflow.

4. Experimental technique and lidar data processing

The experimental data used in the present work were obtained indirectly by estimating the smoke density distribution from lidar curve sets, obtained by scanning the laser beam through real-fire smoke plumes. As stated in the Introduction, the lidar signal contains information about the particle concentration in the smoke plume, which is proportional to the local backscattered radiation power collected by the lidar receiver optics plotted as a function of time. Therefore, a lidar curve represents the temporal dependence of the backscattered radiation power. As in the case of radar, the time t elapsed from the moment of the laser-pulse emission until the detection moment is related to the distance R from the radiation source to the target by the equation $t = 2R/c$ (where c is the velocity of light and the distance is doubled as light traverses the distance twice). Therefore, the temporal dependence of the lidar signal can easily be related to a distance dependence. The distance dependence of the power collected by the lidar receiver, $P_{\text{rec}}(R)$, is given by the lidar equation [9]:

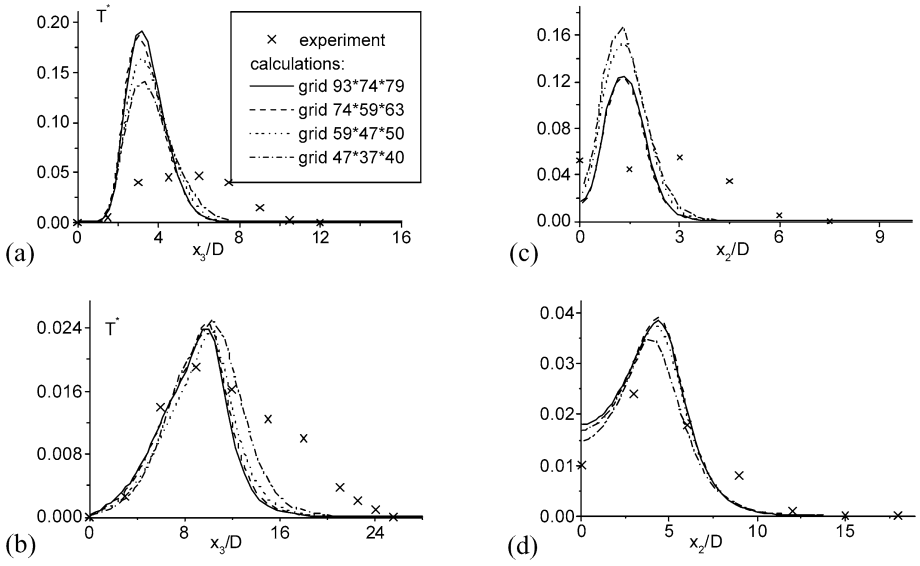

Fig. 2. Experimental [24] and calculated profiles of dimensionless temperature T^* for a hot plume in cross-flow wind: $x_1 = 10D$, $x_2 = 0.05D$ (a), $x_1 = 40D$, $x_2 = 1.69D$ (b), $x_1 = 10D$, $x_3 = 6D$ (c) and $x_1 = 40D$, $x_3 = 9.09D$ (d). Calculations are made for four different non-uniform grids: $47 \times 37 \times 40$, $59 \times 47 \times 50$, $74 \times 59 \times 63$ and $93 \times 74 \times 79$.

$$P_{\text{rec}}(R) = E_l \frac{c\pi D_{\text{rec}}^2}{8R^2} \tau_{\text{rec}} \tau_{\text{tr}} \exp\left(-2 \int_0^R \alpha(R')\,\mathrm{d}R'\right) \beta(R) \quad (10)$$

In this equation E_l is the laser pulse energy, D_{rec} the receiver optics diameter, τ_{rec} the receiver efficiency, τ_{tr} the transmitter efficiency, α the extinction coefficient, and β the backscattering coefficient of the medium.

The boundaries of the smoke plume were defined as the loci of points corresponding to 10% of the maximum lidar signal due to backscattering from smoke particles. The backscattering coefficient distribution, extinction coefficient, and smoke particle concentration distributions were calculated from the lidar curves using Klett's [37,38] lidar signal inversion method.

The variant of Klett's method used includes the following assumptions:

The backscattering coefficient is proportional to α^κ, where the value of constant κ depends on the dominant extinction mechanism:

$$\beta = c_{\beta\alpha}\alpha^\kappa, \quad c_{\beta\alpha} = \text{const}, \quad \kappa = \text{const} \quad (11)$$

The extinction profile is restored within a segment of the laser beam trajectory containing the intersection of the laser beam with the smoke plume and limited by the reference distance R_{fin}, so that $0 \leqslant R \leqslant R_{\text{fin}}$. This reference distance corresponds to the point of the beam situated at the furthest boundary of the smoke plume, where the laser beam exits the plume. For the reference distance the value of the extinction coefficient, $\alpha_{\text{fin}} = \alpha(R_{\text{fin}})$, must be estimated from independent considerations.

Substitution of the backscattered power P by the logarithmic range-adjusted power, defined as $S(R) = \ln(\frac{R^2}{R_{\text{fin}}^2}\frac{P_{\text{rec}}(R)}{P(R_{\text{fin}})})$, enables the lidar equation to be transformed into the ordinary differential equation $\frac{\mathrm{d}S}{\mathrm{d}R} = \frac{1}{\beta}\frac{\mathrm{d}\beta}{\mathrm{d}R} - 2\alpha$, which for $\beta \sim \alpha^\kappa$ reduces to the Bernoulli (homogeneous Riccati) differential equation, yielding an analytical solution in the form

$$\alpha(R) = \frac{\exp(\kappa^{-1}S(R))}{\alpha_{\text{fin}}^{-1} + 2\kappa^{-1}\int_R^{R_{\text{fin}}} \exp(\kappa^{-1}S(R'))\,\mathrm{d}R'} \quad (12)$$

The constant κ depends on the dominant extinction mechanism. In the case of smoke, the main contribution to extinction and backscattering comes from smoke particles, so hereafter both α and β are assumed to be proportional to the smoke particle concentration n

$$\alpha = c_{\alpha n} n, \quad \beta = c_{\beta n} n, \quad c_{\alpha n} = \text{const}, \quad c_{\beta n} = \text{const} \quad (13)$$

and $\kappa = 1$. The extinction coefficient α_{fin} in Klett's equation (13) was estimated using Nilsson's [39] computation results for a visibility of 15 km.

Within the above assumptions, the smoke particle concentration profile $n(R)$ can be estimated from the extinction coefficient profile $\alpha(R)$, restored from the lidar curve with the help of Klett's equation (12):

$$n = \frac{\beta}{c_{\beta n}} = \frac{c_{\beta\alpha}\alpha^\kappa}{c_{\beta n}} = \frac{c_{\beta\alpha}}{c_{\beta n}}\alpha \quad (\kappa = 1) \quad (14)$$

The value of the backscattering-to-extinction ratio, $c_{\beta\alpha} = 0.033\ \text{sr}^{-1}$, was estimated on the basis of experimental [40] and computational [41] data. To estimate the backscattering-to-concentration ratio, which, in the Mie scattering approximation, takes the form [42]

$$c_{\beta n} = \frac{\beta}{n} = \frac{\pi \int_0^\infty r^2 \theta_B(r, \lambda, n^*) N(r)\,\mathrm{d}r}{\int_0^\infty N(r)\,\mathrm{d}r} \quad (15)$$

the experimental particle size distribution $N(r)$ measured by Stith et al. [15] was used. In Eq. (15), θ_B is the Mie backscattering efficiency, r the particle radius, λ the wavelength, and n^* the complex refraction index. The main parameters of the lidar equipment used in the experiments are presented in Table 1.

Table 1
Characteristics of the lidar set-up

Parameter	Units	Value
Laser		
Flashlamp-pumped, water-cooled, Q-switched Nd:YAG		
Repetition rate	Hz	12
Pulse duration	ns	10
Beam divergence	mr	< 0.5
Operating wavelengths	nm	532
Maximum pulse energy	mJ	20
Total transmitter efficiency		0.9
Receiver		
Cassegrainian telescope, lens diameter 30 cm, focal length 156.2 cm		
Effective area	m^2	0.0678
Full angle of field of view	mr	0.9
Efficiency		0.64
Bandwidth	nm	4.8
FEU-83 photomultiplier with Peltier cooling		
Dark current	A	$4 \cdot 10^{-7}$
Gain		$\sim 10^5$
Photocathode responsivity	$mA\,W^{-1}$	0.7
Data acquisition system		
IBM-compatible PC with ISA ADC board		
Distance	km	1–30
Detection length	m	6
On-board data buffer	Kbyte	64

5. Experimental and computational results and comparison

The field experiments were carried out within the framework of the GESTOSA campaign [43]. Experimental data from Viegas et al. [44], Fernandes [45], and Cruz and Viegas [46] were used to calculate the shrub fuel load. Other fire parameters were estimated assuming that the fire area has a rectangular shape, the fire front is a straight line moving with a constant velocity, and the fire was ignited in the upwind corner of the rectangle.

In accordance with the above assumptions, the rectangular fire area may be subdivided into three regions (I, II, and III as shown in Fig. 3), each having a different area burned per unit time. The temporal dependence of the each burning area, S_1, S_2, and S_3, was calculated on the basis of a simple geometrical treatment, using the equations:

$$S_1(t) = c_1 t^2, \quad 0 \leqslant t \leqslant t_{1\,\max} \tag{16}$$

$$S_2(t - t_{1\,\max}) = b_2(t - t_{1\,\max})$$
$$t_{1\,\max} \leqslant t \leqslant t_{1\,\max} + t_{2\,\max} = t_{12\,\max} \tag{17}$$

$$S_3(t - t_{12\,\max}) = b_3(t - t_{12\,\max}) - c_1(t - t_{12\,\max})^2$$
$$t_{12\,\max} \leqslant t \leqslant t_{12\,\max} + t_{3\,\max} = t_{\max} \tag{18}$$

Here $t_{1\,\max}$, $t_{2\,\max}$, and $t_{3\,\max}$ are the total times of burning of the first, second, and third plots, respectively, and c_1, b_2, and b_3 are constants. All these parameters were estimated using the experimental values of the rectangle dimensions, wind direction, and total fire duration $t_{\max}$. Analysis of Eqs. (16)–(18) shows that $\mathrm{MAX}(\frac{dS_1}{dt}, \frac{dS_2}{dt}, \frac{dS_3}{dt}) = \frac{dS_2}{dt}$, $\frac{dS_1}{dt} > 0$, and $\frac{dS_3}{dt} < 0$. Consequently the smoke yield is maximum during the burning of plot II. So, the fire propagation model suggested reflects the experimental fact that the burning rate was not uniform, passing through a maximum between fire ignition and extinction. Since the lidar measurements were performed during the phase of extensive burning (region II), the computations were carried out for the time interval corresponding to plot II combustion. The relevant fire parameters are presented in Table 2.

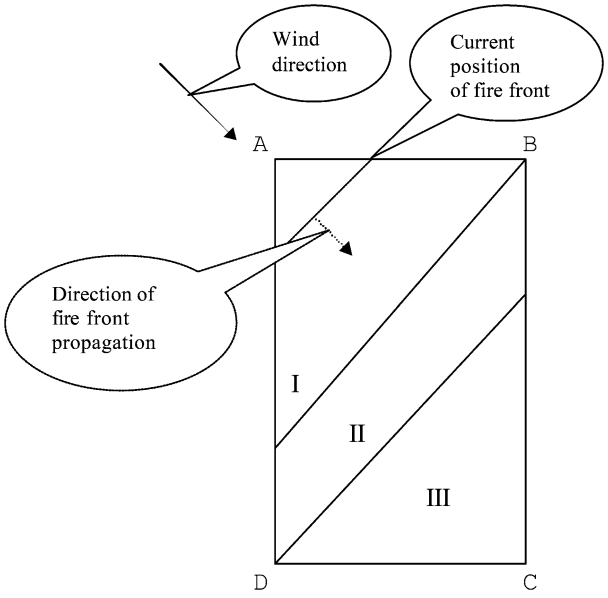

Fig. 3. Scheme of the fire area illustrating wind direction, current position, position of fire front, direction of fire front, and I, II, and III plots of fire area.

Table 2
Parameters of the experimental fire

General parameters			Parameters calculated for plot II (Fig. 2)	
Fire duration, s	Fire area, m^2	Fuel load, $kg\,m^{-2}$	Area burned per unit time, $mm^2\,s^{-1}$	Fuel burnt per unit time, $kg\,s^{-1}$
900	6970	1.5	14.2	21.3

The initial heat release, velocity and temperature were calculated on the basis of thermodynamic considerations discussed by Andreucci and Arbolino [42] and the approximate relationships suggested by Heskestad [47] for large density deficiency. The estimated heat release is 2.7×10^8 $J\,s^{-1}$. Using this value the following boundary conditions were calculated: $u_{\mathrm{jet}} = 17\ m\,s^{-1}$ and $T_{\mathrm{jet}} = 1170$ K. The value of the Froude number is $Fr = 3.5$. From meteorological data $u_{\mathrm{wind}} = 4\ m\,s^{-1}$.

A map of the experimental site is shown in Fig. 4. During the experiments the smoke plume was progressively shifted to the southeast by moderate wind. The lidar was located at an elevated position, approximately 2.4 km southwest to the fire plot. The plume was scanned with zero laser beam elevation, rasterizing the azimuth angle, represented first clockwise, then counter-clockwise. For each beam position, $n_s = 128$ lidar returns were accumulated with a repetition rate of 12 Hz, thus yielding about 10.7 s for the signal accumulation. The laser

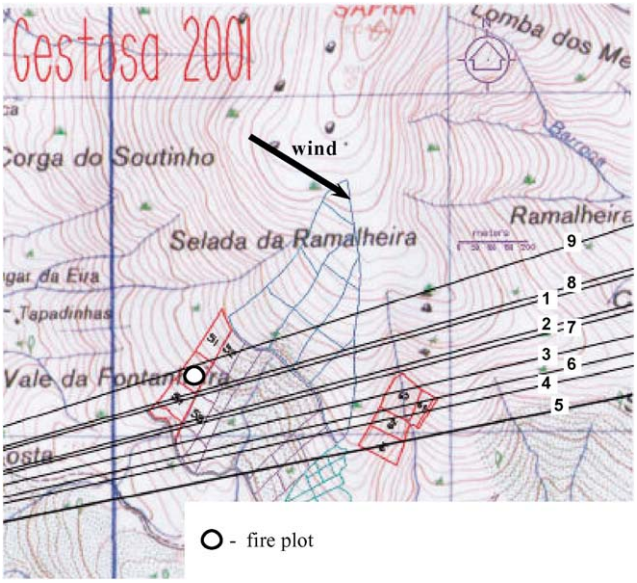

Fig. 4. Map of the experimental site. The solid lines (1)–(9) represent the lidar scanning directions.

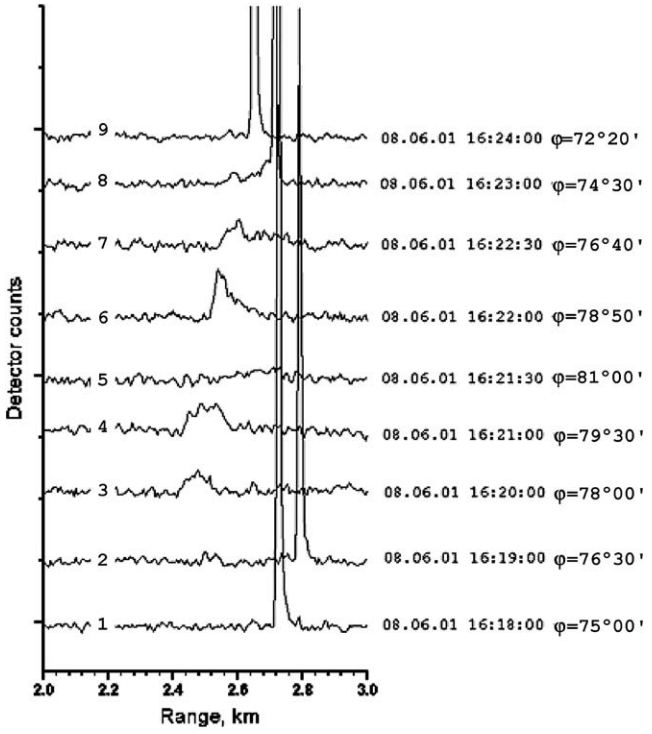

Fig. 5. Raw lidar signals obtained by rasterizing the azimuth angle φ at zero beam elevation (horizontal scanning).

beam directions are shown on the map by a series of straight lines. The corresponding lidar signals are plotted in Fig. 5. The large amplitude peaks visible in some curves correspond to backscattering by the hillside, while the moderate amplitude peaks correspond to the smoke plume. Directions 1, 5, and 9 lie outside the plume boundaries, so the corresponding lidar curves do not exhibit peaks corresponding to backscattering by smoke.

The dimensions of the computational space for the fluid dynamics smoke plume model were $800 \times 275 \times 475$ m^3. Four grids were used in the computations: $45 \times 41 \times 36$, $56 \times 50 \times 45$, $71 \times 63 \times 57$, and $90 \times 82 \times 72$ nodes in the x_1, x_2, and x_3 directions, respectively. Comparison of computations using these grids shows that grid $56 \times 50 \times 45$ secures sufficient accuracy, and the figures hereafter are drawn using this grid.

The inaccuracy of smoke-concentration values calculated from lidar measurement is due to measurement errors and inaccuracies in the parameters used in the calculations ($\alpha_{\text{fin}}, \kappa$, $N(r), n^*$). In the present work, these inaccuracies were estimated using the approach proposed by Laursen et al. [48] and Kovalev and Eichinger [49]. Two important sources of error are inaccuracies in the estimation of α_{fin} and in the choice of the refractive index value [50–52]. Taking into consideration these sources of inaccuracy, an uncertainty of $\pm 70\%$ in the smoke concentrations calculated from the lidar signals can be estimated.

Distributions of smoke particle concentrations n along scanning directions 3, 4, and 6 (see Figs. 4 and 5), calculated from the lidar signals via Klett's method, are shown in Fig. 6. The corresponding calculated distributions are shown in the same plot as dashed, dotted, and dash-dotted curves (for $x_3 = 72$, 78, and 84 m, respectively). The calculations for these three relatively close values of x_3 aim to demonstrate the influence of inaccuracy in the observation point height (which in the lidar experiment is associated with an error in the definition of the laser beam elevation) on the concentration profile.

The distance to the target predicted on the basis of the hydrodynamics model is similar to the experimental value. The maximum values of particle concentration in the calculated profile vary between 80 and 300% of the corresponding experimental values, while calculated plume widths are approximately two times larger than the experimental values. While the smoke particle concentration distribution in Fig. 6(a) presents a double-peak structure, those in Fig. 6(b) and (c) show a single peak. This can be explained by the significant fluctuations in wind velocity and direction occurring during the experiment, which resulted in plume rotation and more pronounced mixing than predicted by the model. In this situation the ten-second averaged lidar returns do not reflect the instantaneous plume structure.

It should be noted that lidar measurements present a relatively simple, but essentially indirect method of assessing smoke particle distribution. Accordingly, the discrepancy between theory and experiment resulting from the theoretical part—inaccuracy of the numeric model (mostly, inherent limitations in description of turbulence and approximation of temperature/velocity equilibrium between the particulate and gas phases), errors in the experimental values of wind direction and velocity used in the calculations, and failure to take into account their fluctuations during the lidar measurements—is aggravated by significant uncertainties of the lidar signal inversion discussed earlier. Even expensive large-scale experiments involving lidar calibration with the help of direct airborne particle measurements yield relative errors of about 50% or worse (see, for example, [53]). Thus the fact that the predicted particle concentration distributions are of the same order as the experimental ones, testifies that the numerical model may be used for the semiqualitative assessment of forest-fire smoke disper-

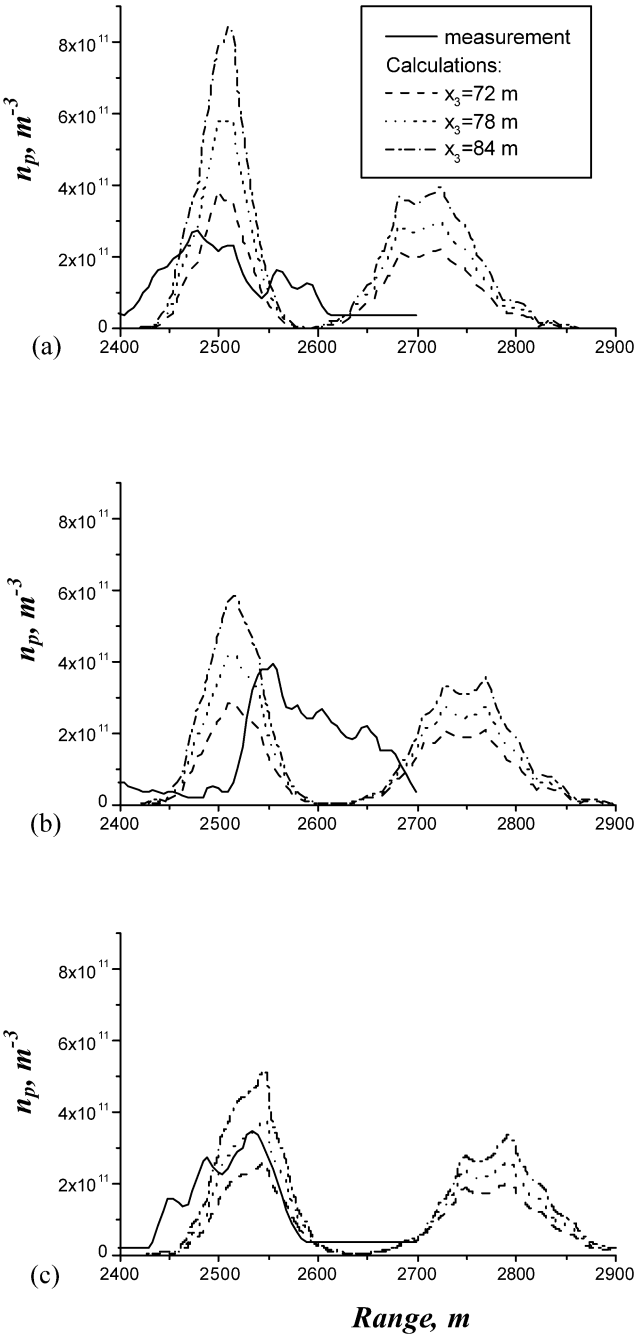

Fig. 6. Distributions of smoke particle concentrations along the lidar scanning direction calculated using lidar measurements ($x_3 = 80$ m) and the gasdynamic model ($x_3 = 72$, 78, and 84 m). Variants (a), (b), and (c) correspond to lidar scanning in directions 3, 6, and 4 shown in Fig. 4.

sion and, in particular, for simulation of training patterns for artificial-intelligence systems of smoke signatures in lidar data sets. On the other hand, it provides evidence that the rapid and easy-to-implement Klett's inversion procedure yields, by means of layer-by-layer lidar scans yields, feasible characteristics of the internal smoke structure, such as the position and shape of the areas of significant smoke-particle concentration, and even gives an estimate of the absolute value of this concentration.

The latter information cannot be obtained using cameras; however it is extremely important for the experimental verification of gasdynamic models of fire propagation and smoke dispersion (the same approach may be used for investigating dispersion of pollutants) as well as for chiefs of fire brigades and supporting air forces: in the case of sufficiently dense smoke covering the fire area and the surroundings, rapid evaluation of lidar scans allows them to "see" the core of the smoke masked by its outer layers.

The dynamics of plume dispersion by wind, as described using the numerical modelling results, is illustrated in Figs. 7–9. For heights above ground between 0 and 50 m, the plume rises practically vertically. The influence of wind cross-flow in this part of the trajectory is small (Fig. 7), because the plume momentum flux prevails over wind forces. In the downwind direction the influence of wind forces becomes dominant: the plume bends and for $x_1 \geqslant 50$ m the rising speed is lower.

Calculated smoke particle isoconcentration lines in horizontal planes at 72, 78, and 84 m above the fire level are shown in Fig. 8. The downwind shift of the plume core is approximately 25 m. The plume is also strongly asymmetric in the wind direction. As a result, the concentration gradient is much higher on the windward side of the plume than on the leeward side.

Smoke particle isoconcentration contours for $x_1 = 104$, 302, and 400 m are shown in Fig. 9. Widening and rising of the plume downstream is clearly observable, as well as its typical kidney-shaped cross-section.

Several additional calculations were made in order to clarify how the wind velocity, buoyancy, and the kinetic energy of wind turbulence influence the plume dynamics. Contours of smoke particles concentration in the vertical symmetry cross-section for various values of u_{wind}, T_{jet}, and k_{air} are presented in Fig. 7. Numerical results of Figs. 7(a), 7(b), and 7(c) are obtained for the wind velocities of 4, 3, and 6 m s^{-1} respectively. It is seen that for $u_{\text{wind}} = 3$ and 4 m s^{-1} the plume rises, accordingly, up to the heights of about 180 and 130 m, while for stronger wind of 6 m s^{-1} the plume is stretched significantly in the wind direction. The influence of buoyancy can be clarified from comparison of results presented in Figs. 7(a) ($T_{\text{jet}} = 1170$ K) and 7(d) ($T_{\text{jet}} = 319$ K), which relate to the density ratios $\frac{\rho_{\text{jet}}}{\rho_{\text{air}}} = 0.25$ and 0.9. It is seen that for the case of the density ratio closer to unity $\frac{\rho_{\text{jet}}}{\rho_{\text{air}}} = 0.9$, i.e., small buoyancy, the plume is stretched significantly in the wind direction and is more dispersed. The plume structures shown in Figs. 7(b) and 7(e) are calculated using, respectively, different turbulent kinetic energy of the ambient air $k_{\text{air}} = 0.04\frac{u_1^2}{2}$ and $0.02\frac{u_1^2}{2}$. It is seen that the two-fold decrease of k_{air} causes only a small displacement of plume. The above comparative calculations demonstrate that, despite the strong influence of the main wind parameters (and hence the error of their definition and their instability) on the plume behaviour, the whole plume structure holds the same qualitative characteristics and is not subjected to abrupt changes for relatively small wind variations.

6. Detection range for smoke plumes

Apart from being a tool for smoke behaviour research, lidar is an efficient instrument for early forest fire detection. In this

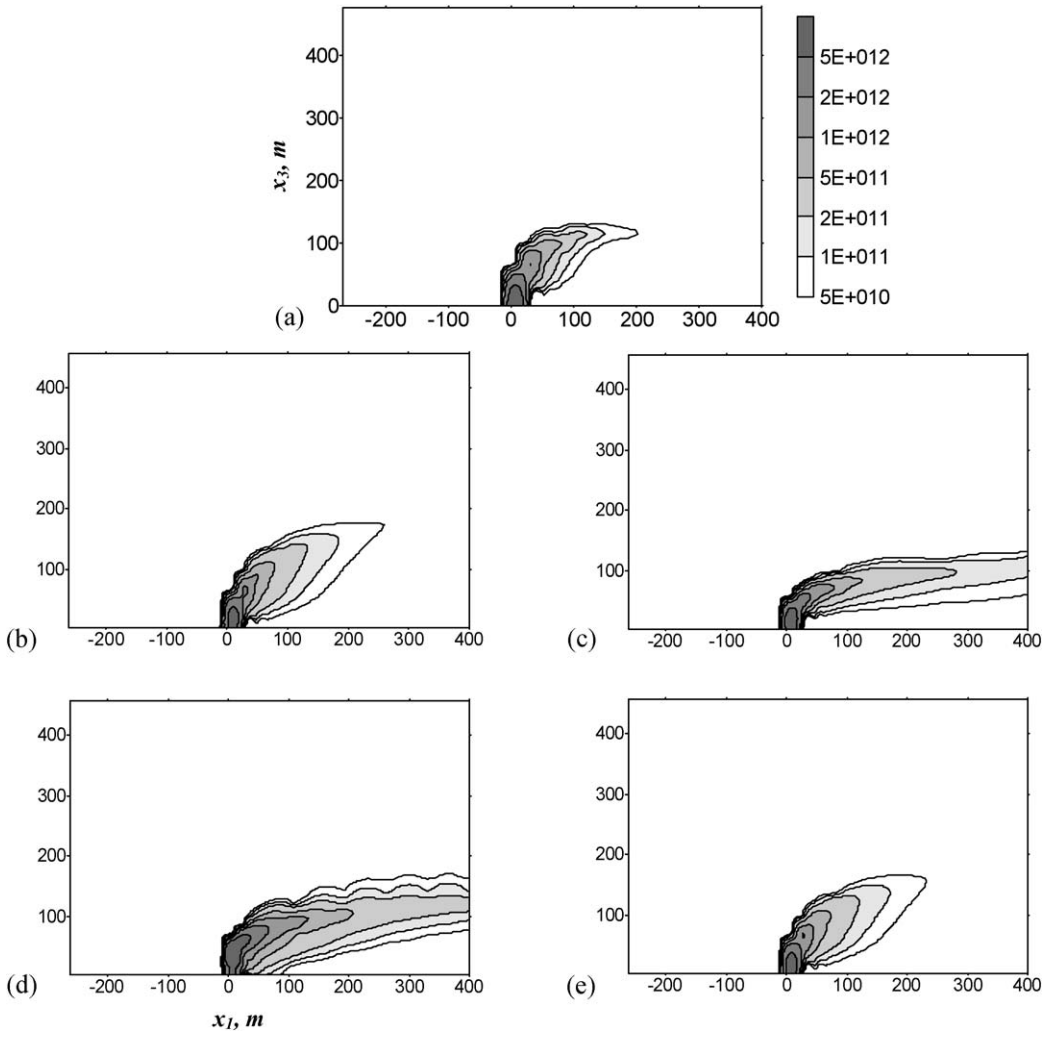

Fig. 7. Contours of smoke particle concentration in the vertical symmetry cross-section calculated with the help of the fluid dynamics model. Minimum and maximum concentrations are 5×10^{10} m^{-3} and 5×10^{12} m^{-3}. The model parameters are: (a) $u_{\text{wind}} = 4$ m s^{-1}, $T_{\text{jet}} = 1170$ K, $k_{\text{air}} = 0.04u_1^2/2$; (b) $u_{\text{wind}} = 3$ m s^{-1}, $T_{\text{jet}} = 1170$ K, $k_{\text{air}} = 0.04u_1^2/2$; (c) $u_{\text{wind}} = 6$ m s^{-1}, $T_{\text{jet}} = 1170$ K, $k_{\text{air}} = 0.04u_1^2/2$; (d) $u_{\text{wind}} = 3$ m s^{-1}, $T_{\text{jet}} = 319$ K, $k_{\text{air}} = 0.04u_1^2/2$; (e) $u_{\text{wind}} = 3$ m s^{-1}, $T_{\text{jet}} = 1170$ K, $k_{\text{air}} = 0.02u_1^2/2$.

section, the range for reliable forest fire detection will be estimated. For forest fire detection, lidar sensors will be installed on the top of hills. As a consequence, the intersection of the laser beam with the smoke plume will be well above ground. The detection range was estimated for the following three points of intersection of the laser beam with the plume:

$x_1 \approx 0$, $x_3 \approx 50$ m (as can be seen from Fig. 7, the plume starts bending at approximately this point),

$x_1 = 104$ m, $\quad x_3 \approx 100$ m

$x_1 = 302$ m, $\quad x_3 \approx 125$ m

Isoconcentration contours for $x_1 = 104$ and 302 m are presented in Fig. 9. As can be seen from Figs. 7–9, the order of magnitude of the plume diameter at these heights is tens of metres. As a result, a method analogous to that developed by Pal et al. [54] will be used to estimate the detection range. The main difficulty in analysing lidar return signals lies in the fact that due to noise (see for example Fig. 5) it is difficult to distinguish a weak smoke signature from noise fluctuations. This problem is particularly significant for distant targets.

According to Measures [9], the equation for the lidar signal-to-noise ratio is:

$$SNR = \frac{P_{\text{rec}} R_{\text{ph}} G \sqrt{n_s}}{\sqrt{2eG^2FB(P_{\text{rec}} R_{\text{ph}} + P_{\text{bgnd}} R_{\text{ph}} + I_{\text{dark}}/G)}} \tag{19}$$

where R_{ph} and G are the photocathode responsivity and the photomultiplier gain, respectively, n_s is the number of accumulated signals, e is the electron charge, F the noise factor associated with the gain, $B = 1/(2t_p)$ the effective bandwidth, P_{bgnd} the power of received background solar radiation, and I_{dark} the dark current. The equation for P_{bgnd} is presented in [10]. Following Pal et al. [54], the algorithm for calculating the smoke plume detection range is based on the comparison of three values:

- Lidar return from the plume area with maximum particle concentration $P_{\text{rec(peak)}}$.

- Lidar return from the boundary between clear air and the region containing smoke particles $P_{\mathrm{rec(bound)}}$.
- Noise level calculated for the plume area with maximum particle concentration.

Using these signals, the value of

$$SNR' = \frac{(P_{\mathrm{rec(peak)}} - P_{\mathrm{rec(bound)}})R_{\mathrm{ph}}G\sqrt{n_s}}{Noise_{\mathrm{peak}}}$$

is calculated for every distance between the lidar and the smoke plume. Here $Noise_{\mathrm{peak}}$ is the denominator of Eq. (19). Furthermore, following the recommendations of Pal et al. [54], it is assumed that reliable detection is possible if $SNR' \geqslant 2$. The variation of SNR' with distance for three values of the height of the intersection points between the laser beam and the smoke plume is presented in Fig. 10. Analysis of this figure and Figs. 7 and 9

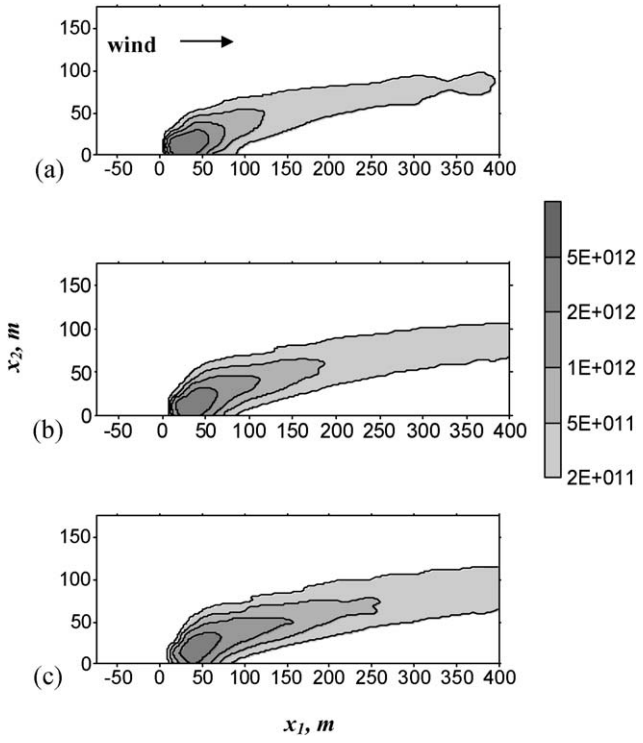

Fig. 8. Contours of smoke particle concentration for the horizontal cross-sections (height $x_3 = 72$, 78, and 84 m for plots (a), (b), and (c), respectively) calculated with the help of the fluid dynamics model. Minimum and maximum concentrations are 2×10^{11} m^{-3} and 5×10^{12} m^{-3}.

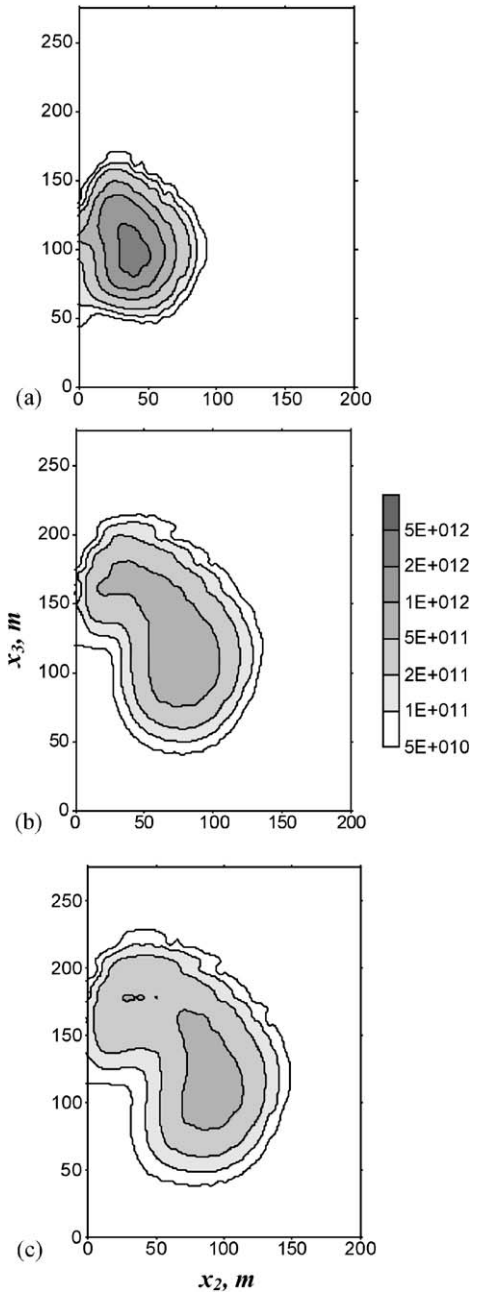

Fig. 9. Contours of smoke particle concentration for three cross-stream sections: $x_1 = 104$, 302, and 400 m for plots (a), (b), and (c) respectively. Minimum and maximum concentrations are 5×10^{10} m^{-3} and 5×10^{12} m^{-3}.

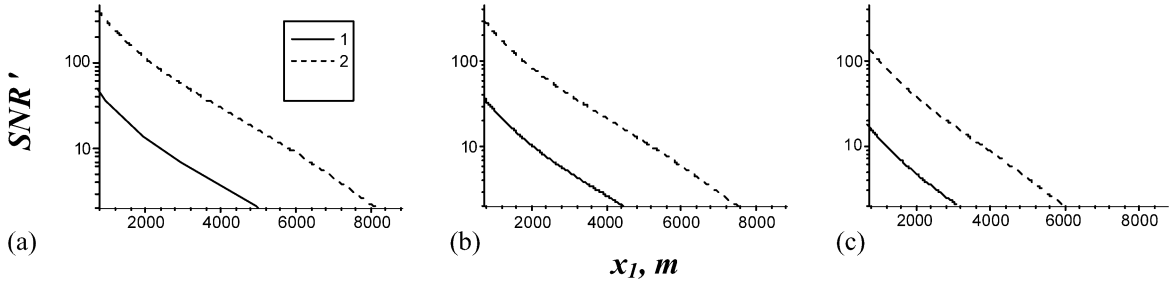

Fig. 10. Dependence of SNR' on distance. The number of accumulated signals n is 4 (1), and 256 (2). The co-ordinates of the laser beam crossing the smoke plume are: $x_1 \approx 0$, $x_3 \approx 50$ m; $x_1 = 104$ m, $x_3 \approx 100$ m; and $x_1 = 302$ m, $x_3 \approx 125$ m ((a), (b), and (c) respectively). Characteristics of the lidar set-up and the experimental fire are presented in Tables 1 and 2, respectively.

shows that a decrease in smoke particle concentration at the intersection point causes a decrease in detection range, which varies between 3 and 8 km depending on the particle concentration and the number of accumulated pulses. A comparison between the present results, based on a three-dimensional model of the plume with cross-wind, with previously published results [6], based on a one-dimensional "top hat" approximation, shows that the one-dimensional model underestimates plume diffusion and consequently overestimates the detection range.

7. Conclusion

Bearing in mind the specificity of the simple indirect lidar-assisted assessment of smoke-plume structure discussed in Section 5, the observed degree of agreement between calculated and reconstructed smoke concentration profiles may be take as satisfactory. It demonstrates that the numerical model based on the three-dimensional system of Navier–Stokes equations developed in the present work adequately describes all essential factors affecting the dispersion of a hot smoke plume in the presence of wind—turbulent mixing, the influence of wind, and the action of buoyancy—and may be used for the semi-qualitative assessment of the evolution of smoke plumes, simulation of training patterns for artificial intelligence systems of smoke recognition on the basis of lidar data sets, and prediction of lidar sensitivity and range with respect to smoke. The comparison of theoretical and experimental data provides additional support for applicability of the rapid lidar-assisted smoke-evaluation method based on Klett's inversion procedure [37,55,56] to analysis of the internal three-dimensional structure of smoke plumes and estimation, at least within an order of magnitude, of the absolute value of smoke-particle concentrations. Much better agreement between computational fluid dynamics and lidar data is anticipated with increased lidar sensitivity due to recent advances in photodetection technology, as it would reduce the data-accumulation time to the characteristic temporal scale of plume perturbations, enabling lidar instruments to make instantaneous snapshots of smoke plumes.

Acknowledgement

The authors wish to thank Prof. X. Viegas of Coimbra University for his help in organizing the field experiments. This research was partially supported by the FOGO project of ADI and by the AGRO project of the Portuguese Ministry of Agriculture.

References

[1] L.E. Drain, The Laser Doppler Technique, John Wiley & Sons, New York, 1980.
[2] R. Sussmann, K. Gierens, Differences in early contrail evolution of two-engine versus four-engine aircraft: Lidar measurements and numerical simulation, J. Geophys. Res. 106 (2001) 4899–4911.
[3] M. Bennett, S. Sutton, D.R.C. Gardiner, An analysis of lidar measurements of buoyant plume rise and dispersion at five power stations, Atmospheric Environment A 26 (1992) 3249–3263.
[4] B. Benech, Dinh Pham Van, A. Ezcurra, Investigation of a 1000 MW smoke plume by means of a 1.064 μm lidar. Determination of diffusion characteristics of the plume particles, Atmospheric Environment 22 (1988) 1071–1084.
[5] T. Mikkelsen, H.E. Jorgensen, M. Nielsen, S. Ott, Similarity scaling of surface-released smoke plumes, Boundary-Layer Meteorology 105 (2002) 483–505.
[6] A. Lavrov, A. Utkin, R. Vilar, A. Fernandes, Application of lidar in ultraviolet, visible and infrared ranges for early forest fire detection, Appl. Phys. B 76 (2003) 87–95.
[7] R.M. Banta, L.D. Olivier, E.T. Holloway, R.A. Kropeli, B.W. Bartram, R.E. Cupp, M.J. Post, Smoke-column observations from two forest fires using Doppler lidar and Doppler radar, J. Appl. Meteorology 31 (1992) 1328–1349.
[8] S. Pershin, W.M. Hao, R.A. Susott, R.E. Babbitt, A. Riebau, Estimation of emission from Idaho biomass fires using compact eye-safe diode lidar, in: A.J. Sedlacek III, K. Wfischer (Eds.), Application of Lidar to Current Atmospheric Topics, III, in: Proc. SPIE, vol. 3757, SPIE, Bellingham, USA, 1999, pp. 60–66.
[9] R.M. Measures, Laser Remote Sensing, John Wiley & Sons, New York, 1984.
[10] A. Utkin, A. Lavrov, L. Costa, F. Simões, R. Vilar, Detection of small forest fires by lidar, Appl. Phys. B 74 (2002) 77–83.
[11] J. Vicente, P. Guillemant, An image processing technique for automatically detecting forest fire, Int. J. Thermal Sci. 41 (2002) 1113–1120.
[12] H.I. Abu-Mulaweh, Experimental investigation of the influence of buoyancy on turbulent flow adjacent to a horizontal plate induced by a trip wire, Int. J. Thermal Sci. 42 (2003) 1013–1020.
[13] R. Dizene, J.-M. Charbonnier, E. Dorignac, R. Leblanc, Étude expérimentale d'une interaction de jets obliques avec un écoulement transversal compressible. I. Effets de la compressibilité en régime subsonique sur les champs aérothermiques, Int. J. Thermal Sci. 39 (2000) 390–403.
[14] K.-H. Baumann, K. Mühlfriedel, Mass transfer and concentration profiles near phase boundaries, Int. J. Thermal Sci. 40 (2001) 425–436.
[15] J.L. Stith, L.F. Radke, P.V. Hobbs, Particle emission and the production of ozone and nitrogen oxides from the burning of forest slash, Atmospheric Environment 15 (1981) 73–82.
[16] S.V. Patankar, Numerical Heat Transfer and Fluid Flow, Hemisphere, Washington, DC, 1980.
[17] A. Bejan, Convection Heat Transfer, John Wiley & Sons, New York, 1984.
[18] V. Novozhilov, Computational fluid dynamics modeling of compartment fires, Progr. Energy Combust. Sci. 27 (2001) 611–666.
[19] S.V. Patankar, D.K. Basu, S.A. Alpay, Prediction of the three-dimension velocity field of a deflected turbulent jet, Trans. ASME J. Fluid Engrg. 99 (1977) 758–762.
[20] L.B.Y. Aldabbagh, I. Sezai, Three-dimensional numerical simulation of an array of impinging laminar square jets with spent fluid removal, Int. J. Thermal Sci. 43 (2004) 241–247.
[21] J.C. Chien, J.A. Schetz, Numerical solution of the three-dimensional Navier–Stokes equations with applications to channel flows and a buoyant jet in cross flow, Trans. ASME J. Appl. Mech. 42 (1975) 575–579.
[22] M.R. Mokhtarzadeh-Dehghan, S. Ergin-Ozkan, A.J. Reynolds, Natural convection between two compartments of a stairwell. Numerical prediction and comparison with experiment, Numer. Heat Transfer Part A 27 (1995) 1–17.
[23] A.O. Demuren, Numerical calculations of steady three-dimensional turbulent jets in cross flow, Comput. Methods Appl. Mech. Engrg. 37 (1983) 309–328.
[24] R.B. Bornoff, M.R. Mokhtarzadeh-Dehghan, A numerical study of interacting buoyant cooling-tower plumes, Atmospheric Environment 35 (2001) 589–598.
[25] K.B. McGrattan, H.R. Baum, R.G. Rehm, Large eddy simulations of smoke movement, Fire Safety J. 30 (1998) 161–178.
[26] X. Zhou, L. Sun, S. Mahalingam, Thermal particle image velocity estimation of fire plume flow, Combust. Sci. Technol. 175 (2003) 1293–1316.
[27] S. Hostikka, K.B. McGrattan, Numerical modeling of pool fires using LES and finite volume method for radiation, in: M.A. Evans (Ed.), Proceedings 7th International Symposium, International Association for Fire Safety Science, Boston, USA, 2003, pp. 383–394.

[28] S. Hostikka, K.B. McGrattan, Large eddy simulation of wood combustion, in: International Interflam Conference, 9th Proceedings, vol. 1, Edinburgh, Scotland, 2001, pp. 755–762.
[29] X. Jiang, K.H. Luo, Dynamics and structure of transitional buoyant jet diffusion flames with side-wall effects, Combust. Flame 133 (2003) 29–45.
[30] F.F. Grinshtein, G.E. Karniadakis, Guest Editorial: Alternative LES and Hybrid RANS/LES for Turbulent Flows, J. Fluid Engrg. 124 (2002) 821–822.
[31] M. Fairweather, W.P. Jones, R.P. Lindstedt, A.J. Marquis, Predictions of a turbulent reacting jet in a cross flow, Combust. Flame 84 (1991) 361–375.
[32] B.E. Launder, D.B. Spalding, The numerical computations of turbulent flows, Comput. Methods Appl. Mech. Engrg. 3 (1974) 269–289.
[33] H. Schlichting, Boundary Layer Theory, McGraw-Hill, New York, 1968.
[34] B. Porterie, J.C. Loraud, D. Morvan, M. Larini, A numerical study of buoyant plumes in cross-flow conditions, Int. J. Wildland Fire 9 (1999) 101–108.
[35] S.P. Patankar, D.B. Spalding, A calculation procedure for heat, mass, and momentum transfer in three-dimensional parabolic flows, Int. J. Heat Mass Transfer 15 (1972) 1787–1806.
[36] CFD for design engineers, CHAM–UK Headquaters, London, 2005, http://www.cham.co.uk.
[37] J.D. Klett, Stable analytical inversion solution for processing lidar returns, Appl. Opt. 20 (1981) 211–220.
[38] V.A. Kovalev, Lidar measurements of the vertical aerosol extinction profiles with range-dependent backscatter-to-extinction ratios, Appl. Opt. 32 (1993) 6053–6065.
[39] B. Nilsson, Meteorological influence on aerosol extinction in the 0.2–40 μm wavelength range, Appl. Opt. 18 (1979) 3457–3473.
[40] D. Althausen, D. Muller, A. Ansmann, U. Wandinger, H. Hube, E. Clauder, S. Zorner, Scanning 6-wavelength 11-channel aerosol lidar, J. Atmospheric Oceanic Technol. 17 (2000) 1469–1482.
[41] Z. Liu, P. Voelger, N. Sugimoto, Simulation of the observation of clouds and aerosols with the experimental lidar in space equipment system, Appl. Opt. 39 (2000) 3120–3137.
[42] F. Andreucci, M.V. Arbolino, A study on forest fire automatic detection systems. 1. Smoke plume model, Nuovo Cimento C 16 (1993) 35–50.
[43] http://www.adai.pt/ceif/Gestosa/.
[44] D.X. Viegas, P.R. Ribeiro, M.G. Cruz, Characterization of the combustibility of forest fuels, in: D.X. Viegas (Ed.), Proceedings of 3rd International Conference on Forest Fire Research, vols. 1, 2, University of Coimbra, Coimbra, Portugal, 1998, pp. 467–482.
[45] P.M. Fernandes, Fire spread modeling in Portuguese shrubland, in: D.X. Viegas (Ed.), Proceedings of 3rd International Conference on Forest Fire Research, vols. 1, 2, University of Coimbra, Coimbra, Portugal, 1998, pp. 611–628.
[46] M.G. Cruz, D.X. Viegas, Fire behavior in some common central Portugal fuel complexes: Evaluation of fire behavior models performance, in: D.X. Viegas (Ed.), Proceedings of 3rd International Conference on Forest Fire Research, vols. 1, 2, University of Coimbra, Coimbra, Portugal, 1998, pp. 859–875.
[47] G. Heskestad, Dynamics of the fire plume, Philos. Trans. Roy. Soc. London A 356 (1998) 2815–2833.
[48] K.K. Laursen, D.G. Baumgardner, B.M. Morley, Optical properties of the Kuwait oil smoke plume as determined using an airborne lidar system: Preliminary results from 28 and 29 May 1991 case studies, Atmospheric Environment 29 (1995) 951–958.
[49] V.A. Kovalev, W.E. Eichinger, Elastic Lidar, John Wiley & Sons, Hoboken, NJ, 2004.
[50] V.S. Kozlov, M.V. Panchenko, Investigation of optical characteristics and particle size distribution of wood-smoke aerosol, Combustion Explosion Shock Waves 32 (1996) 577–588.
[51] L.A. Remer, Y.J. Kaufman, B.N. Holben, A.M. Thompson, D. McNamara, Biomass burning aerosol size distribution and modelled optical properties, J. Geophys. Res. 103 (1998) 31879–31891.
[52] A.A. Isakov, Some results of investigations into the optical and microphysical characteristics of smokes, Atmosph. Oceanic Opt. 12 (1999) 20–27.
[53] A. Ezcurra, B. Benech, Dinh Pham Van, J.L. Lesne, Investigation of a 1000 MW smoke plume by means of a 1.064 μm lidar – I. Lidar calibration procedure from in situ aerosol measurements and vertical lidar shots, Atmospheric Environment 19 (1985) 1125–1133.
[54] S.R. Pal, W.S. Steinbrecht, A.I. Carswell, Automated method for lidar determination of cloud-based height and vertical extent, Appl. Opt. 31 (1992) 1488–1494.
[55] A.B. Utkin, A. Fernandes, F. Simões, A. Lavrov, R. Vilar, Feasibility of forest-fire smoke detection by means of lidar measurements, Int. J. Wildland Fire 12 (2) (2003) 159–166.
[56] A.B. Utkin, A.M. Fernandes, A.V. Lavrov, R.M. Vilar, Eye-safe lidar measurements for detection and investigation of forest-fire smoke, Int. J. Wildland Fire 13 (4) (2004) 401–412.